ELSEVIER

Direct numerical simulation of combined forced and natural turbulent convection in a vertical plane channel

Nobuhide Kasagi and Mitsugu Nishimura
Department of Mechanical Engineering, The University of Tokyo, Tokyo, Japan

The fully developed, turbulent combined forced and natural convection between two vertical parallel plates kept at different temperatures was investigated through a series of direct numerical simulations (DNSs). The pressure gradient drives the mean flow upward, while the buoyant force acts upward (aiding flow) and downward (opposing flow) near the high- and low-temperature walls, respectively. The Reynolds number based on the channel half-width and the friction velocity is assumed to be 150; whereas, the Grashof number based on the channel width and the wall temperature difference varies from 0 to 1.6×10^6. The buoyancy effect on the turbulent statistics including the mean velocity and temperature, the Reynolds stress tensor, and the turbulent heat flux vector are examined. In the opposing flow, the turbulent transport is greatly enhanced with both the Reynolds stresses and the turbulent heat fluxes being remarkably increased; whereas, in the aiding flow, the opposite change is observed. The DNS results presented here are compared with those of the channel flow with uniform wall mass injection and suction (Sumitani and Kasagi 1995) and of the liquid metal channel flow with a transverse magnetic field (Ohtsubo and Kasagi 1992). As a result, it is found that the opposing and aiding buoyancy affects not only the turbulent statistics but also the quasi-coherent structures in much the same way as the wall injection/suction and the Lorenz force. This correspondence should result from the near-wall force balance modified similarly by the additional body force or momentum transport.

Keywords: turbulent convection; direct numerical simulation; combined convection; channel flow; buoyancy; injection; suction; magnetic force

Introduction

Two distinct modes of forced and natural convection often appear combined together in engineering applications and environmental flows. Such a phenomenon often takes place in heat exchangers, turbine blades, solar panels, nuclear reactors, electronic equipment, and silicon processes. Among these types of convective flows, upward flows along heated and cooled vertical walls are, respectively, referred to as aiding and opposing flows, depending upon the combination of the directions of flow and buoyancy. The research work in this area was already initiated in the 1960s (e.g., Metais and Eckert 1964), and since then many experimental investigations have been performed in vertically oriented circular pipes heated from outside, in which a gas or liquid flow was driven downward or upward. These early works mainly examined the heat transfer coefficient, which exhibited peculiar behavior when the buoyancy effect was increased (e.g., Petukhov 1977; Axcell and Hall 1978; Easby 1978; Jackson and Hall 1979; Tanaka et al. 1987). The experimental data accumulated have been correlated into some useful empirical formulas (e.g., Jackson and Fewster 1977; Watt and Chou 1982).

Several reports have attempted to explore the structures of the flow and thermal fields in combined convection flow. Steiner (1971) investigated the mean velocity and temperature profiles of the air flow aided by buoyancy in a vertical pipe, and Easby (1978) investigated those of the nitrogen pipe flow opposed by buoyancy. Nakajima et al. (1980) measured streamwise velocity and temperature fluctuations in aiding and opposing flows, while Carr et al. (1973) obtained velocity and temperature correlations in the aiding flow in a vertical pipe. These experiments show that in the aiding flow, both turbulence and heat transfer rate are decreased despite the increased mean flow velocity, while in the opposing flow, the turbulence activity is enhanced with the mean velocity decreased. A review can be found in Jackson et al. (1989).

Despite the valuable efforts mentioned above, the detailed transport mechanism has not been fully revealed because of the extreme difficulties in experimental measurements, particularly in the vicinity of a wall. With progress in modern technologies, however, extensive knowledge of turbulent combined flow has become ever more desirable. For example, refinement of various computational codes with turbulence models certainly hinges on such knowledge. Hence, the objective of the present study is to obtain detailed statistics of the turbulent combined convection

Address reprint requests to Prof. N. Kasagi, Department of Mechanical Engineering, University of Tokyo, Hongo 7-3-1, Bunkyo-ku, Tokyo 113, Japan.

Received 10 March 1996; accepted 15 October 1996

Int. J. Heat and Fluid Flow 18: 88–99, 1997

655 Avenue of the Americas, New York, NY 10010

0142-727X/97/$17.00
PII S0142-727X(96)00148-8

along a vertical wall and to clarify the effect of buoyancy on the turbulent transport mechanism near the wall. To achieve this, a turbulent vertical channel flow with two different wall temperatures is examined with the aid of direct numerical simulation (DNS). This particular wall thermal condition enables us to investigate the aiding and opposing flows simultaneously; when the mean flow direction is upward, the aiding flow arises on the heated wall, while the opposing flow arises on the cooled wall.

It is known that flows exist when additional forces acting in the flow direction, in which the turbulence is greatly modified, as in combined convection in the vertical channel. For example, in a channel flow with uniform wall injection and suction (e.g., Sumitani and Kasagi 1995) the magnetohydrodynamic (MHD) turbulent flow with the Lorenz force acting in the flow direction (e.g., Shimomura 1991), and the accelerated flow through a converging passage (e.g., Tanaka et al. 1982), the mean momentum or stress balance is drastically changed. Hence, we compare the present DNSs of combined convection with those of injection/suction flow performed by Sumitani and Kasagi and of turbulent MHD flow by Ohtsubo and Kasagi (1992) to discover similar characteristics in the turbulent statistics and structures of these flows.

Numerical procedures

The flow geometry and coordinate system of the vertical channel are shown in Figure 1. The two walls are assumed to be kept at different, but constant temperatures without fluctuations. The Reynolds number Re_τ^* based on the wall friction velocity u_τ^* and the channel half-width δ was set to be 150. Note that u_τ^* is calculated from the wall shear-stress averaged on the two walls. The Grashof number Gr based on the temperature difference between the two walls $\Delta T(=T_h - T_c)$ and the channel width 2δ was changed from 0 to 1.6×10^6, as shown in Table 1. The Prandtl number Pr was assumed to be 0.71. The resultant bulk Reynolds number Re_b based on the channel width in each case is summarized in Table 1. In the present calculations, the Navier–Stokes equations with the Boussinesq approximation, the continuity equation, and the energy equation are used. They are expressed in the following dimensionless forms.

$$\frac{D\tilde{u}}{Dt} = -\frac{\partial}{\partial x}\left(\tilde{p} + \frac{gx}{u_\tau^{*2}}\right) + \frac{1}{\mathrm{Re}_\tau^*}\nabla^2\tilde{u} + \frac{1}{8}\frac{\mathrm{Gr}}{\mathrm{Re}_\tau^{*2}}\left(\tilde{\theta} + \frac{T_c - T_0}{\Delta T}\right) \tag{1}$$

$$\frac{D\tilde{v}}{Dt} = -\frac{\partial\tilde{p}}{\partial y} + \frac{1}{\mathrm{Re}_\tau^*}\nabla^2\tilde{v} \tag{2}$$

$$\frac{D\tilde{w}}{Dt} = -\frac{\partial\tilde{p}}{\partial z} + \frac{1}{\mathrm{Re}_\tau^*}\nabla^2\tilde{w} \tag{3}$$

$$\frac{\partial\tilde{u}}{\partial x} + \frac{\partial\tilde{v}}{\partial y} + \frac{\partial\tilde{w}}{\partial z} = 0 \tag{4}$$

$$\frac{D\tilde{\theta}}{Dt} = \frac{1}{\mathrm{Pr}\,\mathrm{Re}_\tau^*}\nabla^2\tilde{\theta} \tag{5}$$

Notation

B_0 magnetic flux density
b_{ij} Reynolds stress anisotropy tensor, $\overline{u_iu_j}/(2k) - (1/3)\delta_{ij}$
C_f friction coefficient, $C_f = 2\tau_w/\rho\langle U\rangle^2$
c_p specific heat at constant pressure
d distance from the wall to the maximum velocity location
Gr Grashof number, $g\beta\,\Delta T(2\delta)^3/\nu^2$
g gravitational acceleration
Ha Hartmann number, $\mathrm{Ha} = \sqrt{\sigma/\rho\nu}\,B_0\delta$
II second invariant of Reynolds stress anisotropy tensor, $-b_{ij}b_{ji}/2$
III third invariant of Reynolds stress anisotropy tensor, $b_{ij}b_{jk}b_{kl}/3$
k turbulent kinetic energy, $\overline{u_ju_j}/2$
Nu Nusselt number, $2q_wd/(\langle T\rangle - T_w)/\lambda$
Pr Prandtl number, ν/α
p pressure fluctuation
q heat flux
Re_b Reynolds number, $2U_b\delta/\nu$
Re_τ Reynolds number, $u_\tau\delta/\nu$
T temperature
T_0 reference temperature
T_h temperature on the heated wall
T_c temperature on the cooled wall
T_τ friction temperature on each wall, $q_w/\rho c_p u_\tau$
U, V mean velocities
u, v, w fluctuating velocity components in x-, y-, and z-directions
u_τ friction velocity, $\sqrt{\tau_w/\rho}$
u_τ^* friction velocity calculated from the wall shear stress averaged on the two walls
V_0 injection and suction velocity
x, y, z streamwise, wall-normal, and spanwise coordinates

Greek

α thermal diffusivity
β volumetric expansion
ΔT temperature difference, $T_h - T_c$
δ channel half width
ε dissipation rate of k
Θ mean temperature difference normalized by ΔT
Θ_m arithmetic mean temperature over the channel cross section
θ temperature fluctuation normalized by ΔT
λ thermal conductivity
ν kinematic viscosity
ρ density
σ electric conductivity
τ_w wall shear stress

Subscripts

b bulk-averaged over the channel cross section
rms root-mean-square fluctuation
w wall value

Superscripts

$+$ normalized with wall variables on each wall, u_τ, T_τ and ν
$*$ normalized with u_τ^*
$-$ ensemble average over x–z-plane and time
$\sim$ instantaneous value
$\langle\ \rangle$ averaged over d

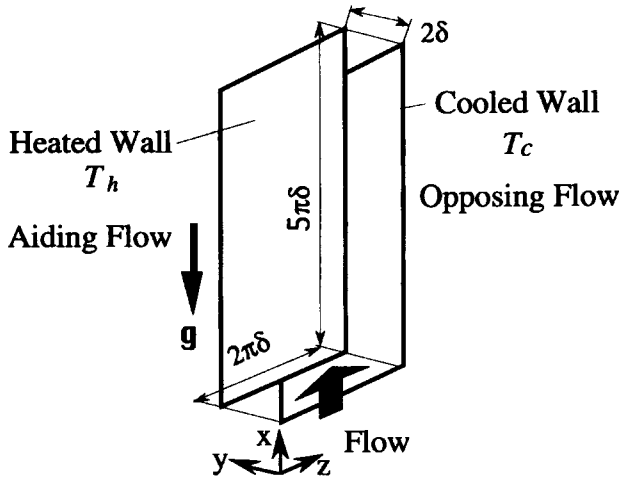

Figure 1 Flow geometry and coordinate system

where T_0 is a reference temperature. The variables in these equations are nondimensionalized by δ, u_τ^*, and ΔT. Referring to the pseudo-spectral method used by Kim et al. (1987), a fourth-order partial differential equation for the wall-normal velocity, a second-order partial differential equation for the wall-normal vorticity, and the continuity and energy equations were used to solve the flow and temperature fields. The collocation grid used to compute the nonlinear terms in physical space had 1.5 times finer resolution in each direction to remove aliasing errors. For time integration, the second-order Adams–Bashforth and Crank–Nicolson schemes were adopted for the nonlinear and viscous terms, respectively. The ordinary no-slip boundary condition was imposed on the velocity components at the walls. The flow and thermal fields were assumed to be fully developed, so that the periodic boundary conditions were imposed at the periods of $5\pi\delta$ and $2\pi\delta$ in the x- and z-directions, respectively.

Four DNSs at different Grashof numbers were performed on relatively coarse grid points; i.e., $64 \times 48 \times 64$ in the x-, y- and z-directions, respectively, by using a workstation (DEC AlphaServer 2100). The time increment in these four cases was $0.4\nu/(u_\tau^*)^2$. Each computation was initially continued for $4800\nu/(u_\tau^*)^2$ until both flow and thermal fields were judged to have reached a fully developed state, and then ensemble averages over space and time were taken for $2400\nu/(u_\tau^*)^2$ (10,000 time steps) in order to obtain various turbulent statistics and their budget. These results are mainly used to examine qualitatively the dependence of the flow characteristics on the imposed buoyancy. Then, in order to obtain the numerical results with sufficient spatial resolution, 128×128 Fourier modes and Chebyshev polynomials up to the 96th order in wavenumber space were used with a time increment of $0.12\nu/(u_\tau^*)^2$ for $Gr = 9.6 \times 10^5$ (Case 3f). This computation was started from the fully developed field in Case 3 and continued for 2400 $\nu/(u_\tau^*)^2$, and then space and time averages were taken for 4800 $\nu/(u_\tau^*)^2$ (40,000 time steps). The computation in this case was carried out on a HITAC-S820/80 supercomputer system at the Computer Center of the University of Tokyo, and for one time step advancement, 3.2s CPU time was required.

Table 1 Flow condition

Case	1	2	3	4
Gr	0.0	6.4×10^5	9.6×10^5	1.6×10^6
Re_b	4358	4341	4328	4148

Case	3f	Kuroda et al. (1994)
Gr	9.6×10^5	0.0
Re_b	4494	4560 ($Re_\tau = 150$)

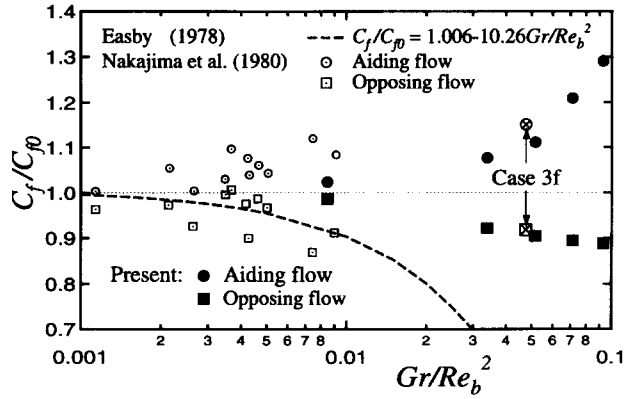

Figure 2 Dependence of normalized friction coefficient on buoyancy effect

Results and discussion

Turbulent statistics in combined convection

Dependence of the friction coefficient and Nusselt number are shown, respectively, in Figures 2 and 3, where the experimental data of Nakajima et al. (1980) and the empirical correlation for the opposing flow proposed by Easby (1978) are also included for comparison. They are calculated by using the following equations:

$$\mathrm{Nu} = 2q_w d/(\langle T \rangle - T_w)/\lambda \tag{6}$$

$$C_f = 2\tau_w/\rho\langle U \rangle^2 \tag{7}$$

where $\langle\ \rangle$ is a bulk-averaged quantity over d, which is the interval from the wall to the maximum velocity location. The friction coefficients and Nusselt numbers in Figures 2 and 3 are normalized by C_{f0} and Nu_0 in Case 1, respectively, except for Case 3f, in which C_{f0} is given from Kuroda et al. (1994). Note that the fine grid simulation of Case 3f gives $C_f = 9.90 \times 10^{-3}$ and Nu = 7.42 for the aiding flow, while $C_f = 7.90 \times 10^{-3}$ and

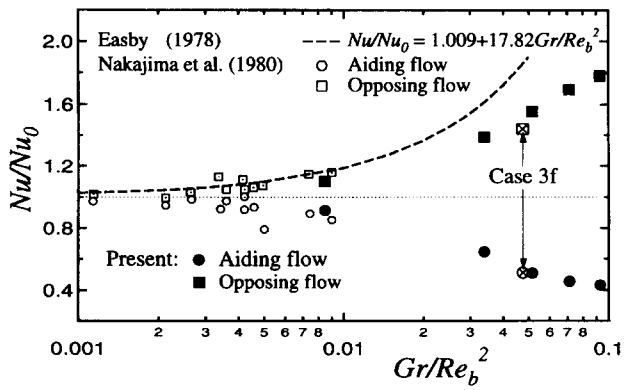

Figure 3 Dependence of normalized Nusselt number on buoyancy effect

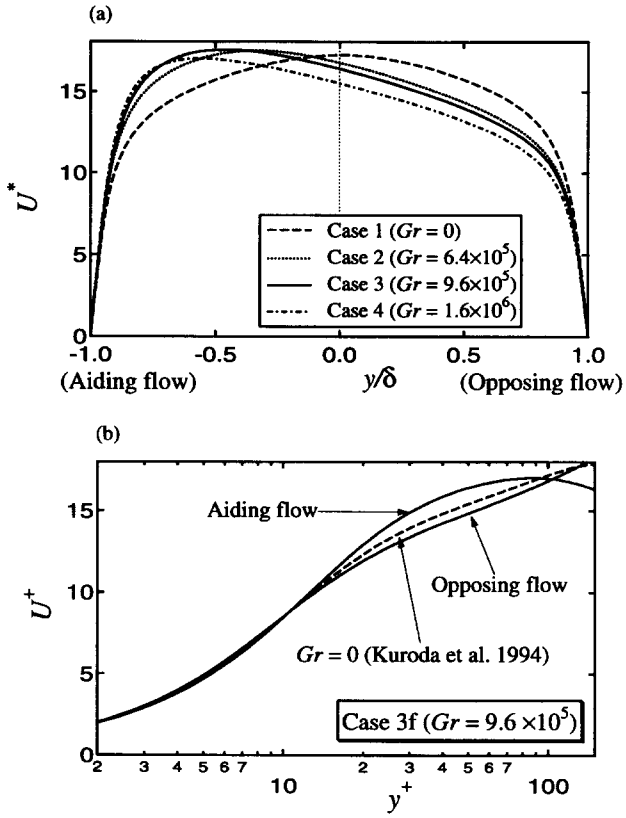

Figure 4 Mean velocity profiles: (a) in global coordinates; (b) in wall coordinates

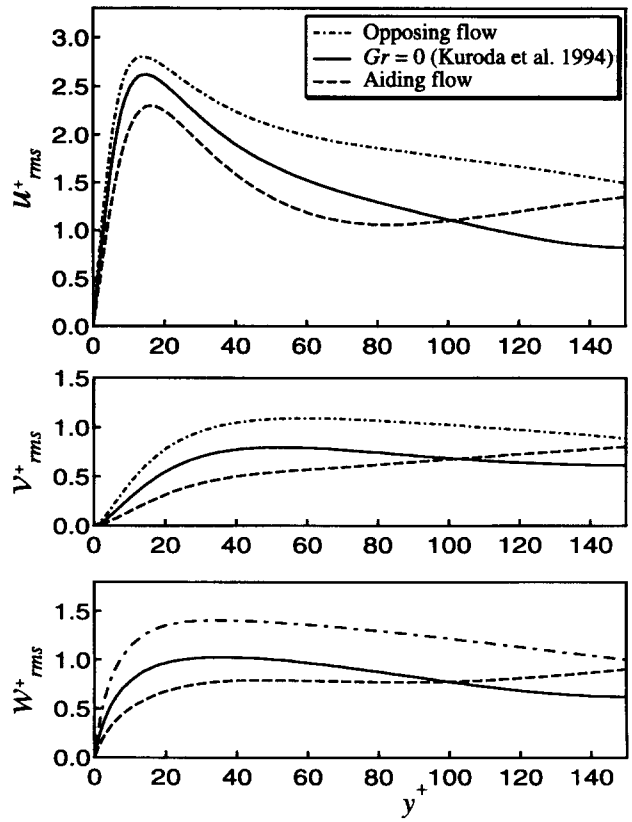

Figure 5 Rms velocity fluctuations (Case 3f)

Nu = 20.94 in the opposing flow. It is evident that the friction coefficient is increased in the aiding flow (on the heated wall), while decreased in the opposing flow (on the cooled wall), with increasing Gr/Re_b^2. However, the Nusselt number exhibits an inverse trend; it is decreased and increased in the aiding and opposing flows, respectively, as the buoyancy force is increased. These facts are in good agreement with the results found in the previous investigations, although the empirical formula of Easby (1978) seems to overpredict the buoyancy effect at large values of Gr/Re_b^2.

The mean velocity profiles in global coordinates are shown in Figure 4a. It is evident that the velocity profile becomes more asymmetric as Gr is increased. The mean velocity profiles of Case 3f in the wall plot are shown in Figure 4b. Note that the superscript $^+$ denotes the quantity nondimensionalized by the wall friction velocity defined on each wall. In the aiding flow, the logarithmic region no longer exists, and U^+ is much larger than the velocity profile of Gr = 0, which was calculated by Kuroda et al. (1994). On the other hand, the logarithmic profile shifts downward in the opposing flow.

The rms velocity fluctuations near the walls are shown in Figure 5. In the aiding flow, they are decreased. However, because the reduction of v^+_{rms} and w^+_{rms} is much larger than that of u^+_{rms}, the Reynolds stress anisotropy is enhanced. In the opposing flow, all three components are increased with the anisotropy weakened. The near-wall distribution of the Reynolds shear stress is shown in Figure 6, where a drastic change with buoyancy is observed. Owing to the stress balance modified by the imposed buoyancy, as discussed later, the Reynolds shear-stress diminishes markedly in the aiding flow, while it increases in the opposing flow.

Figures 7a and b show the mean temperature profiles in the global and wall coordinates, respectively. The mean temperature profile in the global coordinates also becomes asymmetric with increasing Gr, and the mean temperature gradient becomes larger in the aiding flow, while it becomes smaller in the opposing flow. In addition, the mean temperature Θ^+ in the wall coordinates exhibits a systematic change with the imposed buoyancy; the profile shifts upward in the aiding flow and downward in the opposing flow as the mean velocity profile. These results are in good accordance with the experimental data of Nakajima et al. (1980). Figure 8 shows the rms temperature fluctuations. They are only slightly decreased and increased in the near-wall region ($y^+ < 10$) in the aiding and opposing flows, respectively, as the velocity fluctuations. On the other hand, the temperature fluctuation away from the wall exhibits an opposite change; it is increased in the aiding flow and decreased in the opposing flow. This is because the temperature gradient becomes steeper (see

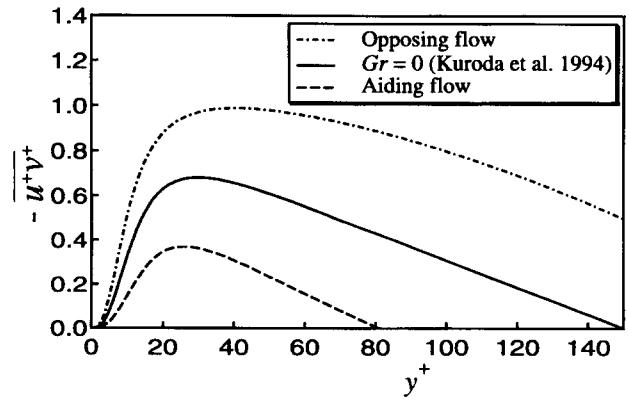

Figure 6 Reynolds shear stress (Case 3f)

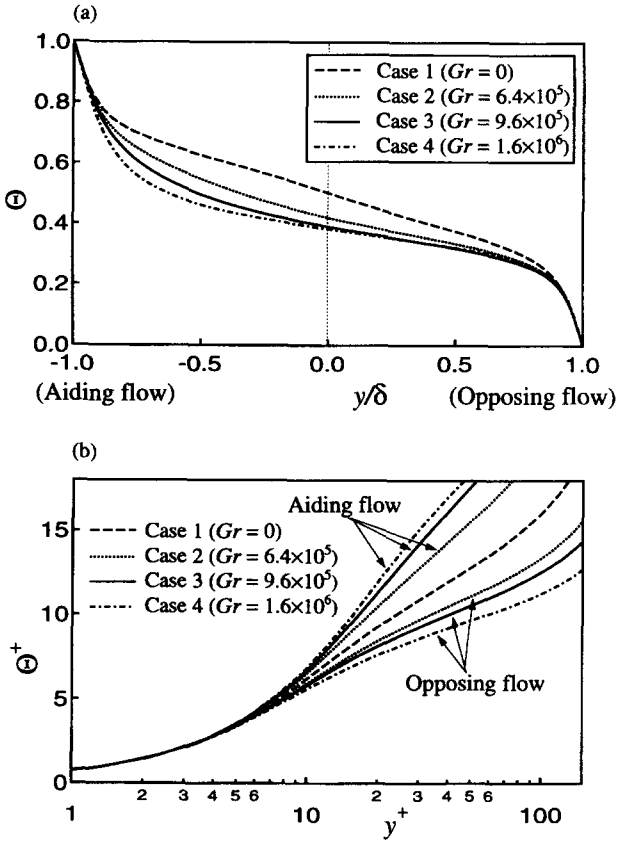

Figure 7 Mean temperature profiles: (a) in global coordinates; (b) in wall coordinates

Figure 7b) and makes the production rate of θ^+_{rms} larger in the aiding flow.

The two components and orientation of the turbulent heat flux vector are shown in Figure 9. When Gr increases, the wall-normal component is increased and decreased in the opposing and aiding flows, respectively, as the Reynolds shear stress in Figure 6. This fact is consistent with the Nusselt number shown in Figure 3. However, the change in the wall-normal heat flux is moderate when compared with that in the Reynolds shear stress. Although the streamwise component is also influenced considerably and in a little more complex way, the vector orientation exhibits a systematic change with Gr; i.e., the heat flux vector near the wall is more aligned with the mean flow direction in the aiding flow. Note that the heat flux vector should be exactly

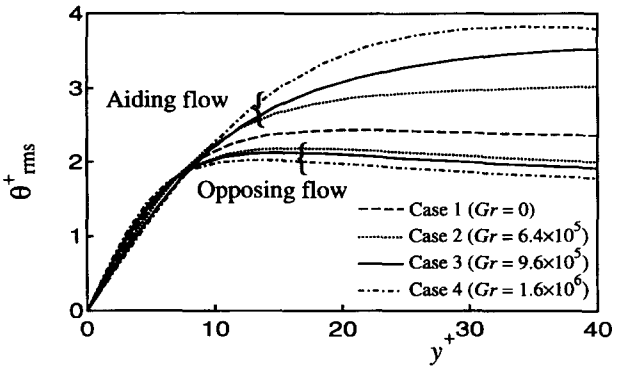

Figure 8 Rms temperature fluctuations

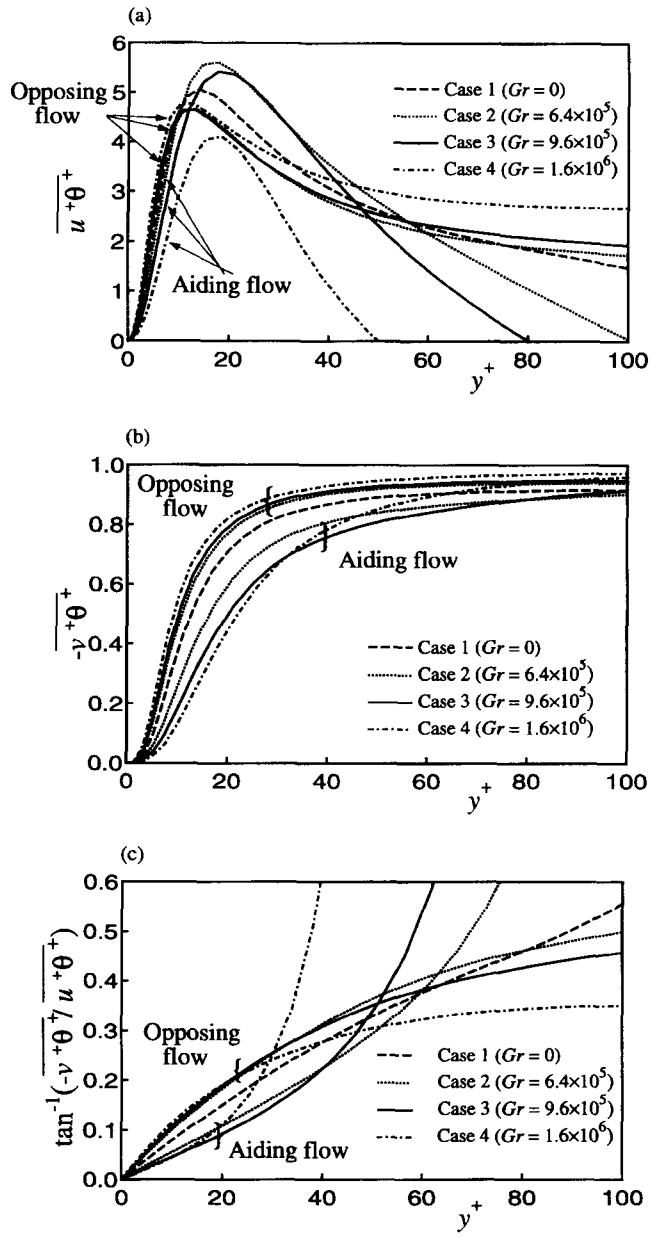

Figure 9 Turbulent heat flux vector: (a) streamwise component; (b) wall-normal component; (c) orientation

aligned with the wall-normal direction at some point in the channel central region, where the streamwise component is zero.

The stress balance and the budget of velocity fluctuations are discussed in the following. By integrating the streamwise mean momentum equation from the wall to y^*, we obtain the following equation for the stress balance:

$$\frac{dU^*}{dy^*} - \overline{u^* v^*} + \frac{\mathrm{Gr}}{\mathrm{Re}_\tau^{*3}} \int_0^{y^*} (\Theta - \Theta_m)\, dy^* = \left.\frac{dU^*}{dy^*}\right|_{y^*=0} - \frac{y^*}{\mathrm{Re}_\tau^*} \tag{8}$$

where Θ_m denotes the arithmetic mean (not bulk-mean) temperature averaged over the channel cross section. The three terms on the left-hand side of Equation 8 are the viscous stress, the Reynolds shear stress, and the buoyant force, respectively, and

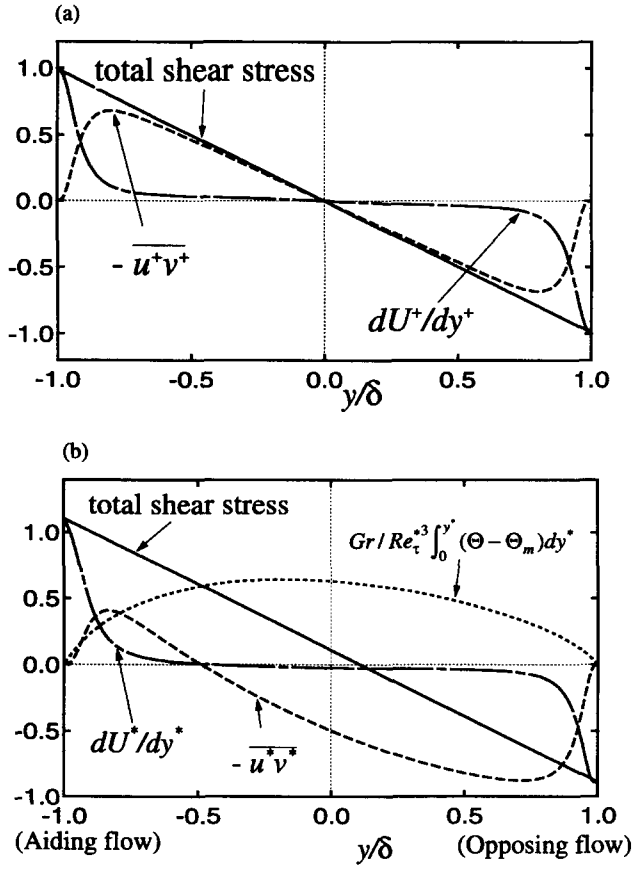

Figure 10 Stress balance: (a) isothermal flow (Kuroda et al. 1994); (b) combined convection flow (Case 3f)

the sum of these balances with the pressure gradient on the right-hand side. Each term in Equation 8 for Gr = 0 and Gr = 9.6×10^5 is shown in Figures 10a and b. In the isothermal flow, there is no buoyancy term, and the symmetrically distributed viscous and Reynolds shear stresses balance with the streamwise pressure gradient. However, in the combined convection in the vertical channel, these stress distributions are deformed asymmetrically because of the buoyancy term imposed. This modification of the near-wall Reynolds stress distribution has been shown to be the major cause for the turbulence suppression or activation in the combined convective flows by previous investigators; e.g., Tanaka et al. (1982, 1987). Note that, although the total and viscous stresses are only slightly changed, the Reynolds shear stress is drastically changed and becomes highly asymmetric.

In the fully developed channel flow, the budget equation of the turbulent kinetic energy k^+ is given as:

$$0 = \underbrace{-\overline{u^+v^+}\frac{\partial U^+}{\partial y^+}}_{\text{Shear production}} \underbrace{-\frac{1}{2}\frac{\partial}{\partial y^+}\overline{u_i^+u_i^+v^+}}_{\text{Turbulent diffusion}} \underbrace{+\frac{\partial^2 k^+}{\partial y^{+2}}}_{\text{Viscous diffusion}}$$

$$\underbrace{-\frac{\partial}{\partial y^+}\overline{p^+v^+}}_{\text{Pressure diffusion}} \underbrace{-\overline{\frac{\partial u_i^+}{\partial x_j^+}\frac{\partial u_i^+}{\partial x_j^+}}}_{\text{Dissipation}} \underbrace{+\frac{\mathrm{Gr}}{\mathrm{Re}_\tau^{*3}}\overline{u^+\theta}}_{\text{Production by buoyancy}} \qquad (9)$$

Figure 11 shows each term in Equation 9. Note that the vertical axis in Figure 11a is enlarged twice that in Figure 11b. It is now clear that the shear production term is markedly changed owing to the Reynolds shear stress distribution modified by the buoyancy; the shear production is decreased in the aiding flow and increased in the opposing flow, respectively. The other terms show similar behavior. Note that the production term attributable to buoyancy in Equation 9 is much smaller than the shear production and has a negligible effect in the present range of Gr. This is also the case for the budgets of the three turbulent kinetic energy components as well as the Reynolds shear stress, although not shown here. Thus, the buoyancy force does not affect the turbulent fluctuations directly; whereas, its effect on the mean flow field plays a dominant role. This is unlike the horizontal shear flows under density stratification (see, e.g., Iida and Kasagi 1995), where the pressure correlation (pressure–strain and pressure-diffusion) and turbulent diffusion terms in each of the budget equations of the Reynolds stress and heat flux are also markedly affected. These distinct characteristics in vertical and horizontal flows are consistent with the qualitatively different coupling manners of the Reynolds stresses and scalar fluxes in these flows discussed by Launder (1984).

Dynamical similarity of the effect of buoyancy in vertical channel flow with those of wall injection/suction and magnetohydrodynamic force

It is known that in the flow with wall injection, the turbulence is increased and the mean velocity is decreased, as in the opposing flow. On the other hand, in the suction flow and the liquid metal MHD flow with a transverse magnetic field, the turbulent activity

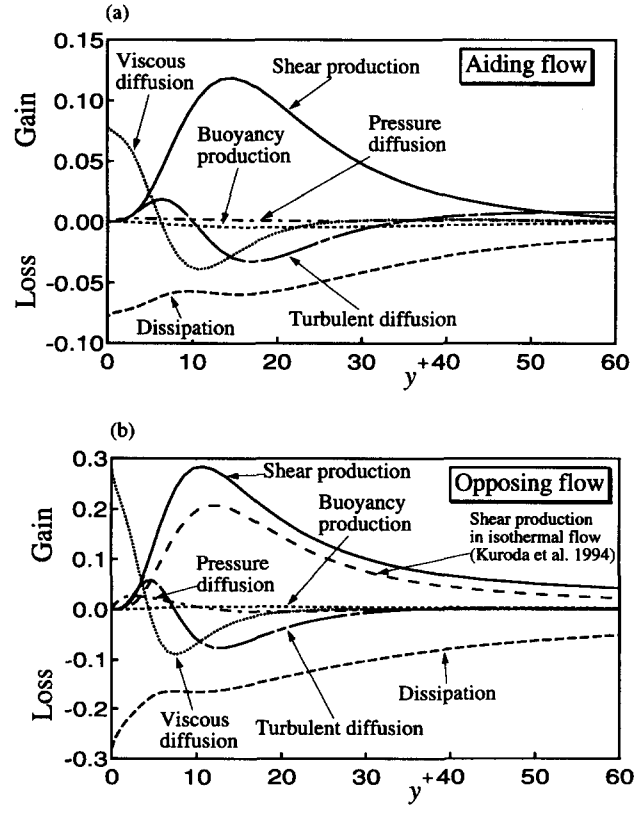

Figure 11 Budget of turbulent energy in combined convection: (a) aiding flow; (b) opposing flow (Case 3f)

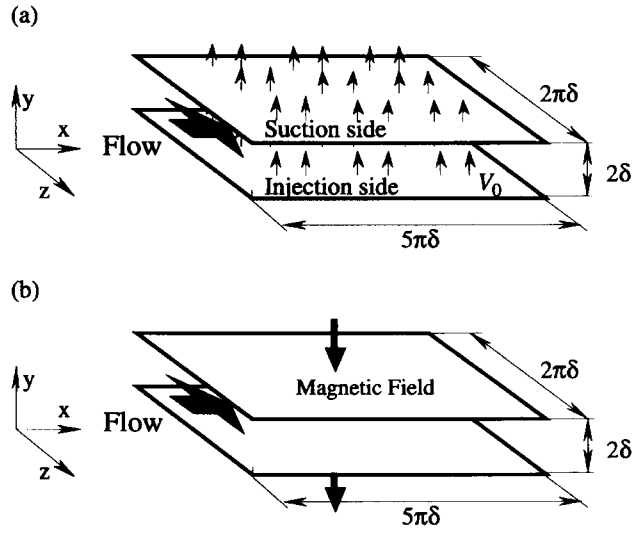

Figure 12 (a) Channel flow with uniform wall injection and suction; (b) MHD channel flow with transverse magnetic field

is reduced and the mean velocity is increased as in the aiding flow. Hereafter, we compare the present results of the combined convection in the vertical channel (Case 3f) with those of the channel flow with uniform wall injection/suction and of the liquid metal MHD channel flow under a uniform transverse magnetic field to discover some similar or common characteristics of the turbulent statistics and the turbulent structures. The latter DNS data to be compared are the injection and suction flow obtained by Sumitani and Kasagi (1995) and the MHD channel flow by Ohtsubo and Kasagi (1992). These flows are shown schematically in Figure 12.

In Figure 12a, the injection and suction are given normal to two walls. A dimensionless parameter V_0^* $(=V_0/u_\tau^*)$, which specifies the strength of injection and suction, is 0.05. In the MHD flow, the magnetic field is imposed normal to the walls, so that the Lorenz force damps the velocity components in the plane parallel to the wall, as shown in Figure 12b. The dimensionless parameter, which indicates the Lorenz force strength, is known as the Hartmann number $\mathrm{Ha} = \sqrt{\sigma/\rho\nu}\,B_0\delta$, where σ and B_0 are the electric conductivity and the magnetic flux density, respectively. In the DNS of Ohtsubo and Kasagi (1992), the Hartmann number was 4. These DNSs have been performed at $\mathrm{Re}_\tau^* = 150$ using $128 \times 96 \times 128$ grid points as in the combined convection (Case 3f).

Table 2 Bulk Reynolds number and friction coefficient

Flow	Re_b	C_f
Standard channel flow (Kuroda et al. 1994)	4560	8.64×10^{-3}
Combined convection (Case 3f)	4494	9.90×10^{-3} (Aiding) 7.90×10^{-3} (Opposing)
Injection and suction (Sumitani and Kasagi 1995)	4357	1.25×10^{-2} (Suction) 6.29×10^{-3} (Injection)
MHD flow (Ohtsubo and Kasagi 1992)	4610	8.51×10^{-3}

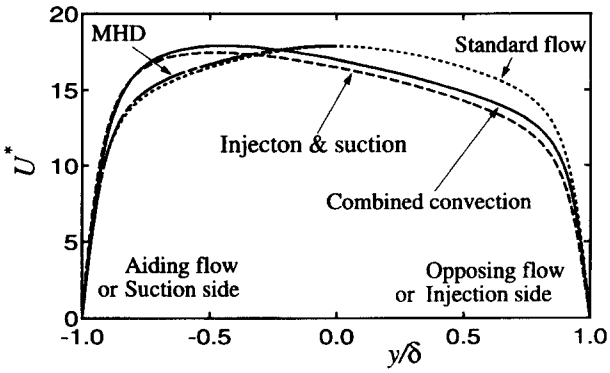

Figure 13 Distributions of mean velocities

The bulk Reynolds numbers Re_b and friction coefficients C_f (defined by Equation 7) in these flows are summarized in Table 2, and the mean velocity profiles and turbulent kinetic energy are shown in Figures 13 and 14, respectively. In the aiding, suction, and MHD flows, where the turbulent energy is decreased, the mean velocities are increased. On the other hand, in the opposing and injection flows, where the turbulent energy is increased, the mean velocities are considerably decreased. However, in the aiding and suction flows the friction coefficient is increased because of steeper mean velocity gradients, whereas in the opposing and injection flows it is decreased.

The turbulence state can be examined in terms of the invariants of the Reynolds stress anisotropy tensor, $b_{ij} = \overline{u_i u_j}/2k - \delta_{ij}/3$. Figures 15a, b, and c represent the second and third invariants, and the angle between the wall and one of the principal axes on the Reynolds stress tensor, respectively. The second invariant of $-II$ is zero if turbulence is isotropic, whereas it takes the largest possible value of $1/3$ when turbulence has only one nonzero component (Lumley and Newman 1977). In Figure 19a, a marked change in $-II$ appears, depending upon the dynamical influence imposed. When the turbulence is activated or attenuated, $-II$ decreases or increases, respectively, because of the change in the redistribution mechanism of turbulent energy from the streamwise component to two other ones. It should be mentioned that the enhanced anisotropy has also been observed in the channel flow simulations at low Reynolds numbers (Kasagi and Shikazono 1995). Hence, the phenomena observed in the aiding, suction, and Hartmann flows can be identified as a low-Reynolds number effect. Also note that the wall-

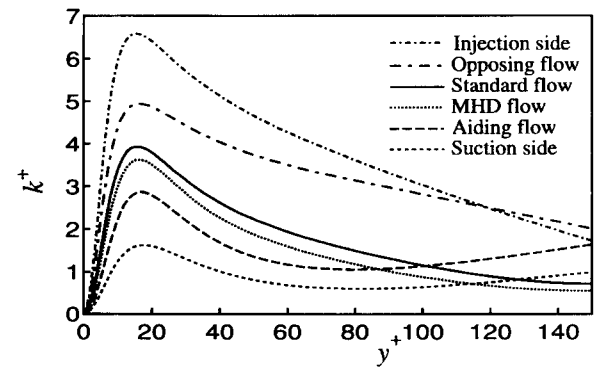

Figure 14 Distributions of turbulent kinetic energy

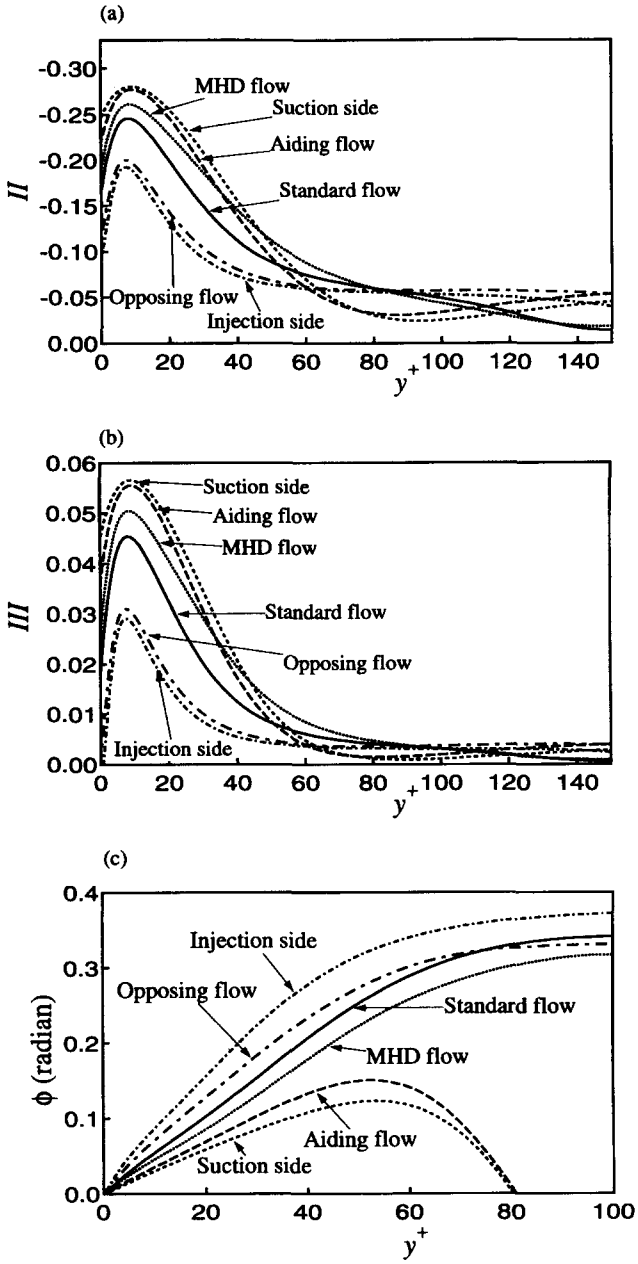

Figure 15 Anisotropy tensor of Reynolds shear stress: (a) second invariant; (b) third invariant; (c) orientation of principal axis

limiting value of *II* is appreciably affected. This fact must be handled properly in modeling the near-wall turbulence.

The third invariant of *III* in Figure 15b is an index of whether a component is larger or smaller than the other two. It takes the smallest value of $-1/108$ when a component is zero and the two other components are equal, while it becomes the largest of $2/27$ when two components are zero. The change in *III* is very similar to that in *II*. The principal axis of the Reynolds stress also exhibits a systematic change that it is more and less aligned with the streamwise direction when the turbulence is attenuated and activated, respectively.

The momentum (stress) balance of the injection/suction flow and that of the MHD flow are shown in Figures 16a and b, respectively, to investigate the effects of the imposed force on

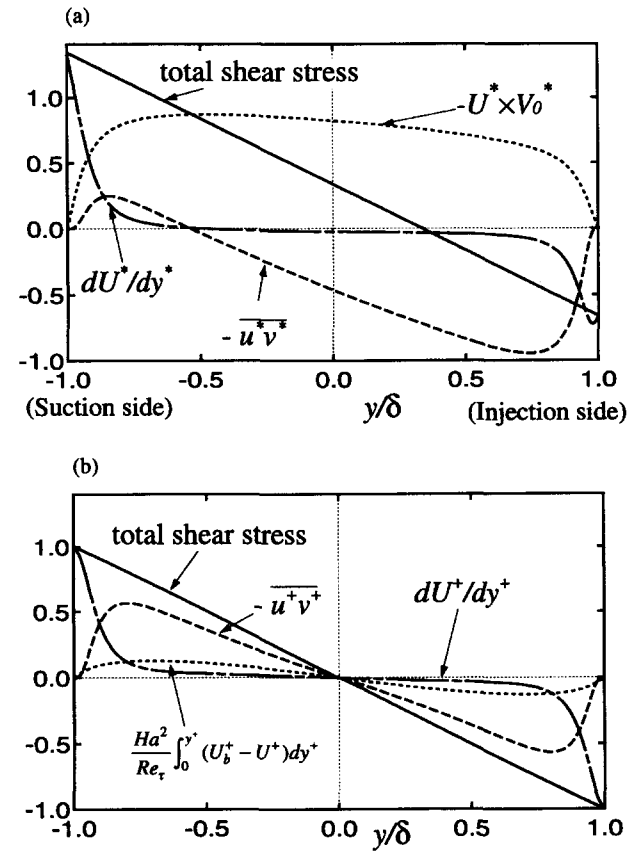

Figure 16 Stress balance: (a) channel flow with injection and suction (Sumitani and Kasagi 1995); (b) MHD channel flow (Ohtsubo and Kasagi 1992)

the mean flow field. The following equations can be derived.

$$\frac{dU^*}{dy^*} - \overline{u^*v^*} - U^* \times V_0^* = \left.\frac{dU^*}{dy^*}\right|_{y^*=0} - \frac{y^*}{\mathrm{Re}_\tau^*} \tag{10}$$

$$\frac{dU^+}{dy^+} - \overline{u^+v^+} + \frac{\mathrm{Ha}^2}{\mathrm{Re}_\tau}\int_0^{y^+}(U_b^+ - U^+)\,dy^+ = \left.\frac{dU^+}{dy^+}\right|_{y^+=0} - \frac{y^+}{\mathrm{Re}_\tau} \tag{11}$$

The additional terms induced by the injection/suction and the Lorenz force appear as the third terms on the left-hand side of Equations 10 and 11 as in the stress balance Equation 8 for the combined convection. These additional terms also modify the distribution of the Reynolds shear stress drastically, as seen in both Figures 16a and b. As a result, the Reynolds shear stress is decreased in the suction and MHD flows and increased in the injection flow. Thus, the effects of the injection/suction and of the Lorenz force on the mean flow are dynamically similar to that of the buoyancy force in the vertical combined convection.

The budget of the turbulent kinetic energy k^+ in the injection/suction and MHD flows are shown in Figure 17. The budget equations in these flows are, respectively, given as follows:

$$0 = \underbrace{-\overline{u^+v^+}\frac{\partial U^+}{\partial y^+}}_{\text{Shear production}} \underbrace{-\frac{1}{2}\frac{\partial}{\partial y^+}\overline{u_i^+u_i^+v^+}}_{\text{Turbulent Diffusion}} \underbrace{+\frac{\partial^2 k^+}{\partial y^{+2}}}_{\text{Viscous diffusion}}$$

$$\underbrace{-\frac{\partial}{\partial y^+}\overline{p^+v^+}}_{\text{Pressure diffusion}} \quad \underbrace{-\overline{\frac{\partial u^+}{\partial x_j^+}\frac{\partial u_i^+}{\partial x_j^+}}}_{\text{Dissipation}} \quad \underbrace{-V_0\frac{\partial k^+}{\partial y^+}}_{\text{Convection}} \tag{12}$$

$$0 = \underbrace{-\overline{u^+v^+}\frac{\partial U^+}{\partial y^+}}_{\text{Shear Production}} \quad \underbrace{-\frac{1}{2}\frac{\partial}{\partial y^+}\overline{u_i^+u_i^+v^+}}_{\text{Turbulent Diffusion}} \quad \underbrace{+\frac{\partial^2 k^+}{\partial y^{+2}}}_{\text{Viscous diffusion}}$$

$$\underbrace{-\frac{\partial}{\partial y^+}\overline{p^+v^+}}_{\text{Pressure diffusion}} \quad \underbrace{-\overline{\frac{\partial u_i^+}{\partial x_j^+}\frac{\partial u_i^+}{\partial x_j^+}}}_{\text{Dissipation}}$$

$$\underbrace{+\mathrm{Ha}^2\overline{\left(\frac{\partial \varphi^+}{\partial z^+}u^+ - \frac{\partial \varphi^+}{\partial x^+}w^+\right)}}_{\text{MHD1}} \quad \underbrace{-\mathrm{Ha}^2(\overline{u^+u^+}+\overline{w^+w^+})}_{\text{MHD dissipation}} \tag{13}^{\dagger}$$

In the injection/suction flow, there is the convective term reflecting the wall injection and suction in Equation 12, but it is negligible except in the vicinity of the wall, as seen in Figures 17a and b. In the MHD flow, there are two terms originating from the Lorenz force; one of these terms (MHD1) contributes to the production of turbulent energy, whilst the other term (MHD dissipation) is a sink term. The values of these two terms, however, are much smaller than other terms; see Figure 17c. Again, it is the shear production that is most drastically changed in the injection/suction and MHD flows, because the Reynolds shear stresses are modified by the additional terms in the mean flow field, as shown in Figure 16. Thus, the injection/suction and the Lorenz force have substantial effects on the mean flow, modify the Reynolds stress distributions, and change the shear production, but they have little effect on the velocity fluctuations directly. This mechanism is essentially the same as that observed in the combined convection.

The quasi-coherent turbulent structures in the apparently different channel flows above are discussed below. The low-speed streak and low-pressure region near the wall are shown in Figure 18. The 3-D contour surfaces of streamwise velocity and pressure fluctuations are produced at the thresholds of $u/(u_{\mathrm{rms}})_{\max} = -1.3$ and $p/(p_{\mathrm{rms}})_{\max} = -2.0$, respectively. The visualized zone has a dimension of 1916 and 766 wall units in the x- and z-directions, respectively. As indicated by Robinson (1991) and Kasagi et al. (1995), the strongly negative pressure regions correspond to the turbulent vortical structures, which generate most of the Reynolds stress through the ejection and sweep around them. In the standard channel flow of Figure 18a, typical inclined streamwise vortices of a banana-shape are observed most frequently with some arch-like vortical structures in the near-wall region, as has been reported by Robinson and Kasagi et al. We can also clearly see the streaky structures, which are fairly periodic in the spanwise direction. The corresponding turbulent structures in the opposing and injection flows are shown in Figure 18b and c, respectively, where their appearances seem very much similar. The streamwise vortical structures are observed more frequently and in smaller scale. The activities of vortices are enhanced, and the low-speed streaks become thinner and shorter with activated meandering than those in the standard channel flow. Moreover, the turbulent structures in the aiding and suction flows are also similar, as seen in Figures 18d and e.

† In Equation 13, φ is a scalar quantity defined by the equation: $\nabla^2\varphi = \mathrm{Re}_\tau \nabla\cdot(\mathbf{u}\times\mathbf{B})$.

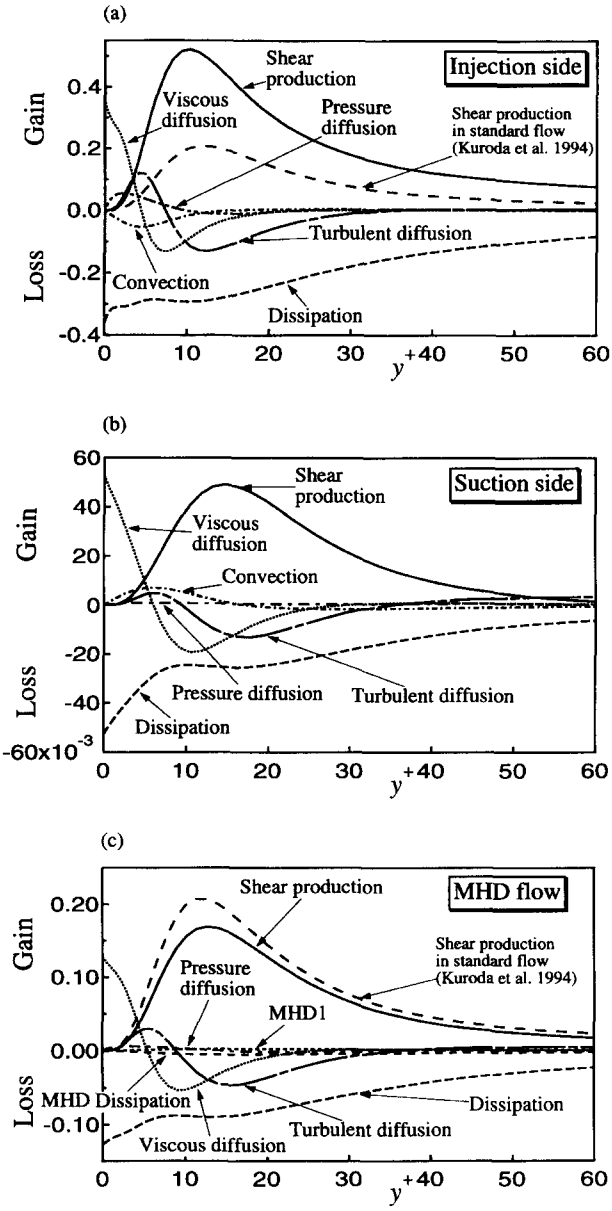

Figure 17 Budget of turbulent kinetic energy: (a) injection side, (b) suction side; (c) MHD channel flow

In these flows, where the turbulence is suppressed, the vortices become weak and appear less frequently and in larger scales, as compared with those in the opposing and injection flows. The low-speed streaks become thick and very long, appearing straighter in the flow direction.

Figure 19 shows the streamwise two-point correlation of the streamwise velocity fluctuations u near the wall. These correlations naturally diminish with distance x^+, but slowly in the aiding, suction, and MHD flows, while quickly in the opposing and injection flows. This result also suggests that the streaky structures become more elongated in the aiding, suction, and MHD flows, while shortened in the opposing and injection flows.

Conclusions

The DNS of the combined force and natural turbulent convection in a vertical channel were performed. The following conclusions have been made.

The buoyancy force has a substantial effect on the mean flow field near the wall. It drastically changes the near-wall force balance, which rules the distribution of the Reynolds shear stress, and then the shear production rate of turbulent kinetic energy. This mechanism has been pointed out in previous investigations, but it is confirmed quantitatively by the present DNSs. For the most part, through this modified shear production, we see that buoyancy can also affect the turbulent fluctuations, but not through direct interaction with them. As the buoyancy force is increased, all the Reynolds stress components and the wall-normal turbulent heat flux are decreased and increased in the aiding and opposing flows, respectively. In the aiding flow, the anisotropy of the Reynolds stress is enhanced with its principal axis as well as the heat flux vector near the wall becoming more aligned with the mean flow direction, whereas the opposite trend is observed in the opposing flow. This must be attributable to the fact that the turbulence redistribution process has also been modified by the enhanced and attenuated turbulence activity.

From extensive comparison with previous DNS results of channel flows under other types of dynamical effects, such as wall mass transfer and a magnetic field, it is found that opposing and aiding buoyancy affect not only the turbulent statistics but

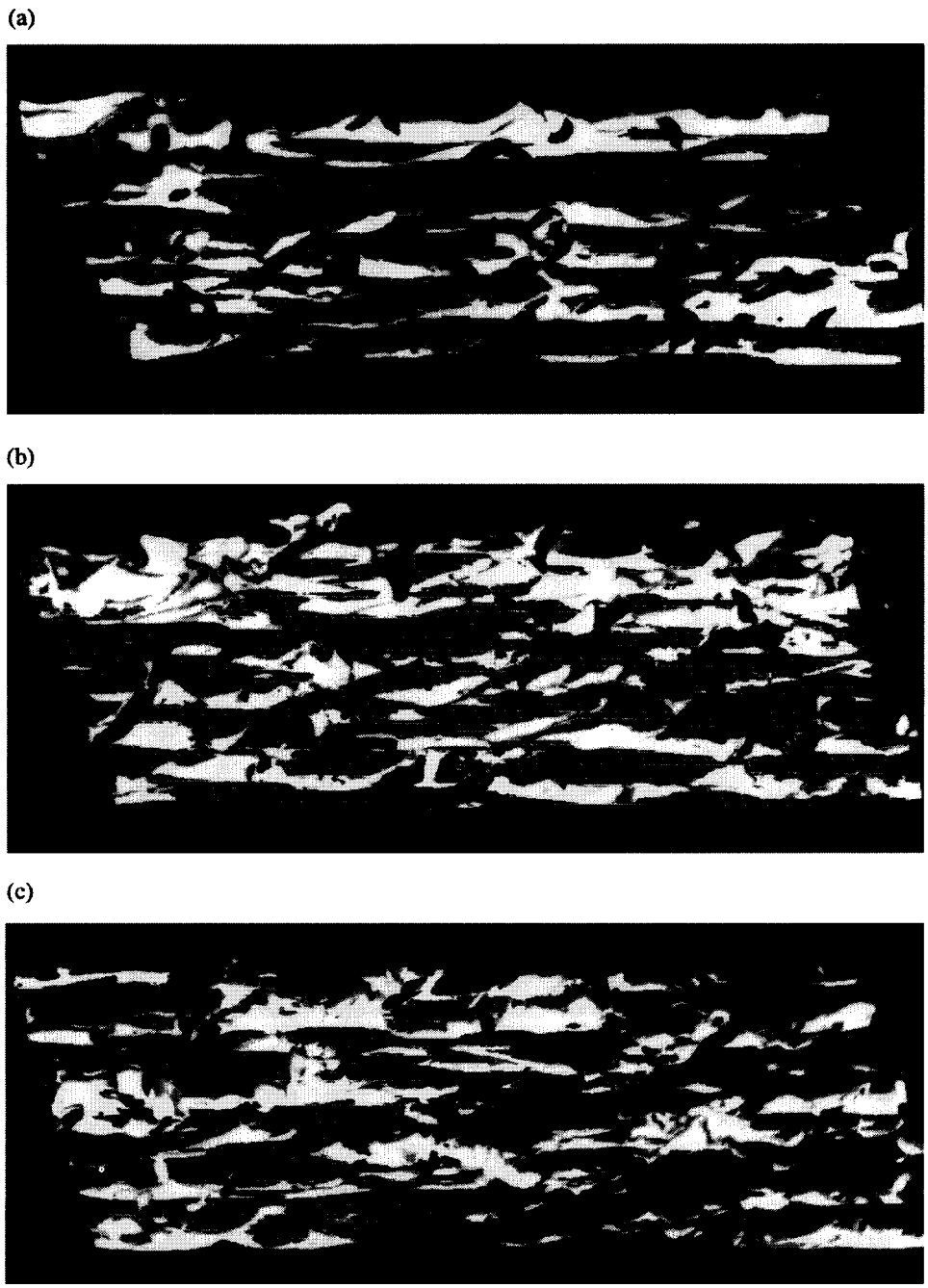

Figure 18 Contours of low-speed streaks and vortical structures ($\Delta x^+ \times \Delta z^+ = 1916 \times 766$); white: $u/(u'_{rms})_{max} = -1.3$, low-speed steak, grey: $p/(p^+_{rms})_{max} = -2.0$, low-pressure region: (a) standard channel flow [$(u^+_{rms})_{max} = 2.62$, $(p^+_{rms})_{max} = 1.75$]; (b) opposing flow [$(u^+_{rms})_{max} = 2.80$, $(p^+_{rms})_{max} = 2.97$]; (c) injection side [$(u^+_{rms})_{max} = 3.21$, $(p^+_{rms})_{max} = 4.02$]; (d) aiding flow [$(u^+_{rms})_{max} = 2.30$, $(p^+_{rms})_{max} = 1.16$]; (e) suction side [$(u^+_{rms})_{max} = 1.73$, $(p^+_{rms})_{max} = 0.68$]

(d)

(e)

Figure 18 (continued)

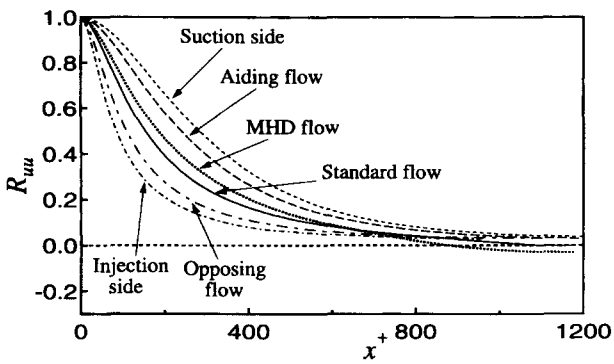

Figure 19 Streamwise two-point correlation of streamwise velocity fluctuations at $y/\delta = 0.03$

also the quasi-coherent structures in much the same way as the wall injection/suction or the Lorenz force. This correspondence should result from the common mechanism; i.e., the near-wall force balance modified by the additional body force or momentum transport.

Acknowledgments

This work was supported through the Grant-in-Aid for Priority Areas (No. 05240103) by the Ministry of Education, Science, and Culture.

References

Axcell, B. P. and Hall, W. B. 1978. Mixed air convection to air in a vertical pipe. *Proc. 6th Int. Heat Transfer Conf.*, Vol. 1, Toronto, 37–42

Carr, A. D., Connor, M. A. and Buhr, H. O. 1973. Velocity, temperature, and turbulence measurements in air for pipe flow with combined free and forced convection. *J. Heat Transfer*, **95**, 445–452

Easby, J. P. 1978. The effect of buoyancy on flow and heat transfer for a gas passing down a vertical pipe at low turbulent Reynolds number. *Int. J. Heat Mass Transfer*, **21**, 791–801

Iida, O. and Kasagi, N. 1995. Direct numerical simulation of unstably stratified turbulent channel flow. *Proc. 4th ASME/JSME Thermal Engineering Joint Conference* Vol. 1, Hawaii, 417–424; also to appear in *J. Heat Transfer*, 1997

Jackson, J. D. and Hall, W. B. 1979. Influences of buoyancy on heat transfer to fluids flowing in vertical tubes under turbulent conditions. In *Turbulent Forced Convection in Channels and Bundles*, Vol. 2, S. Kakac and D. B. Spaulding (eds.), Hemisphere, Bristol, PA, 613–640

Jackson, J. D. and Fewster, J. 1977. Enhancement of turbulent heat transfer due to buoyancy for downward flow of water in vertical tubes. In *Heat Transfer and Turbulent Buoyant Convection*, Vol. 2, D. B. Spaulding and N. Afgan (eds.), Hemisphere, Bristol, PA, **2**, 759–775

Jackson, J. D., Cotton, M. A. and Axcell, B. P. 1989. Studies of mixed convection in vertical tubes. *Int. J. Heat Fluid Flow*, **10**, 2–15

Kasagi, N. and Shikazono, N. 1995. Contribution of direct numerical simulation to understanding and modelling turbulent transport. *Proc. R. Soc. Lond. A*, **45**, 257–292

Kasagi, N., Sumitani, Y., Suzuki, Y. and Iida, O. 1995. Kinematics of the quasi-coherent vortical structure in near-wall turbulence. *Int. J. Heat Mass Transfer*, **16**, 2–10

Kim, J., Moin, P. and Moser, R. 1987. Turbulent statistics in fully developed channel flow at low-Reynolds number. *J. Fluid Mech.*, **177**, 133–166

Kuroda, A., Kasagi, N. and Hirata, M. 1994. Direct numerical simulation of turbulent plate Couette-Poiseuille flow: Effects of mean shear rate on the near-wall turbulence structures. In *Turbulent Shear Flows*, Vol. 9, Springer, Berlin, 241–258

Launder, B. E. 1984. Second-moment closure: Methodology and practice. In *Turbulence Models and Their Applications*, Vol. 2, Eyrolles, Paris, 1–147

Lumley, J. L. and Newman, G. R. 1977. The return to isotropy of homogeneous turbulence. *J. Fluid Mech.*, **82**, 161–178

Metais, B. and Eckert, E. R. G. 1964. Forced, mixed, and free convection regimes. *J. Heat Transfer*, **86**, 295–296

Nakajima, M., Fukui, K., Ueda, H. and Mizushina, T. 1980. Buoyancy effects on turbulent transport in combined free and forced convection between vertical parallel plates. *Int. J. Heat Mass Transfer*, **23**, 1325–1336

Ohtsubo, Y. and Kasagi, N. 1992. Direct numerical simulation of liquid metal MHD turbulence, *Proc. 24th Symposium on Turbulence*, Japan. Soc. Fluid Mech., 67–73 (in Japanese)

Petukhov, B. S. 1977. Turbulent flow and heat transfer in pipes under considerable effect of thermogravitational forces. In *Heat Transfer and Turbulent Buoyant Convection*, Vol. 2, D. B. Spalding and N. Afgan (eds.), Hemisphere, Bristol, PA, 701–717

Robinson, S. K. 1991. The kinematics of turbulent boundary layer structure. NASA TM 103859

Steiner, A. J. 1971. On the reverse transition of a turbulent flow under the action of buoyancy force. *J. Fluid Mech.*, **47**, 503–512

Sumitani, Y. and Kasagi, N. 1995. Direct numerical simulation of turbulent transport with uniform wall injection and suction. *AIAA J.*, **33**, 1220–1228

Shimomura, Y. 1991. Large-eddy simulation of magnetohydrodynamic turbulent channel flows under a uniform magnetic field. *Phys. Fluids A*, **3**, 3098–3106

Tanaka, H., Kawamura, H., Tateno, A. and Hatamiya, S. 1982. Effect of laminarization and retransition on heat transfer for low Reynolds number flow through a converging to constant area duct. *J. Heat Transfer*, **104**, 363–371

Tanaka, H., Maruyama, S. and Hatano, S. 1987. Combined forced and natural convection heat transfer for upward flow in a uniformly heated vertical pipe. *Int. J. Heat Mass Transfer*, **30**, 165–174.

Watt, M. J. and Chou, C. T. 1982. Mixed convection heat transfer to supercritical pressure water. *Proc. 7th Int. Heat Transfer Conf.*, Munich, **3**, 495–500